The effect of interstitial pressure on therapeutic agent transport: coupling with the tumor blood and lymphatic vascular systems

Min Wu[a,+], Hermann B. Frieboes[b,+], Mark A.J. Chaplain[c], Steven R. McDougall[d], Vittorio Cristini[e], and John Lowengrub[*a,f]

[a]Department of Mathematics, University of California, Irvine
[b]Department of Bioengineering and James Graham Brown Cancer Center, University of Louisville
[c]Division of Mathematics, University of Dundee, Dundee, Scotland, UK
[d]Institute of Petroleum Engineering, Heriot-Watt University, Edinburgh, Scotland, UK
[e]Departments of Pathology and Chemical Engineering, University of New Mexico, Albuquerque
[f]Biomedical Engineering Department, University of California, Irvine
[+]Joint first authorship

March 19, 2014

Abstract

Vascularized tumor growth is characterized by both abnormal interstitial fluid flow and the associated interstitial fluid pressure (IFP). Here, we study the effect that these conditions have on the transport of therapeutic agents during chemotherapy. We apply our recently developed vascular tumor growth model which couples a continuous growth component with a discrete angiogenesis model to show that hypertensive IFP is a physical barrier that may hinder vascular extravasation of agents through transvascular fluid flux convection, which drives the agents away from the tumor. This result is consistent with previous work using simpler models without blood flow or lymphatic drainage. We consider the vascular/interstitial/lymphatic fluid dynamics to show that tumors with larger lymphatic resistance increase the agent concentration more rapidly while also experiencing faster washout. In contrast, tumors with smaller lymphatic resistance accumulate less agents but are able

[*]Corresponding author: lowengrb@math.uci.edu

to retain them for a longer time. The agent availability (area-under-the curve, or AUC) increases for less permeable agents as lymphatic resistance increases, and correspondingly decreases for more permeable agents. We also investigate the effect of vascular pathologies on agent transport. We show that elevated vascular hydraulic conductivity contributes to the highest AUC when the agent is less permeable, but leads to lower AUC when the agent is more permeable. We find that elevated interstitial hydraulic conductivity contributes to low AUC in general regardless of the transvascular agent transport capability. We also couple the agent transport with the tumor dynamics to simulate chemotherapy with the same vascularized tumor under different vascular pathologies. We show that tumors with an elevated interstitial hydraulic conductivity alone require the strongest dosage to shrink. We further show that tumors with elevated vascular hydraulic conductivity are more hypoxic during therapy and that the response slows down as the tumor shrinks due to the heterogeneity and low concentration of agents in the tumor interior compared with the cases where other pathological effects may combine to flatten the IFP and thus reduce the heterogeneity. We conclude that dual normalizations of the microenvironment - both the vasculature and the interstitium - are needed to maximize the effects of chemotherapy, while normalization of only one of these may be insufficient to overcome the physical resistance and thus leads to sub-optimal outcomes.

1 Introduction

Chemotherapy is a type of cancer treatment that targets cancer cells through the use of toxic agents, primarily drug molecules disrupting some aspect of cell division, such as DNA synthesis and function. Ideally, drug dosages should be sufficient to kill rapidly dividing tumor cells but not affect non-cancerous cells. Although isolated infusion is sometimes used to deliver a concentrated dosage more directly to specific tumor sites [Chreech *et al.*, 1958, Noorda *et al.*, 2007, McClaine *et al.*, 2012], most drugs are delivered systemically as an oral or intravenous bolus. Tissues in the body that undergo cell proliferation under normal circumstances, such as cells in the digestive system, are also typically damaged by chemotherapeutic drugs. Consequently, the drug dose is usually the maximum tolerated dose (MTD) that prevents patient death but may be well below what is needed to eradicate all of the tumor cells. Diverse macromolecule agents (e.g., nanoparticle carriers as summarized in [Jong & Borm, 2008]) have been developed as vehicles to encapsulate drugs in order to achieve higher targeting efficacy while minimizing systemic toxicity. Nevertheless, both free drug and nanoparticles administered systematically suffer from impaired transport through tumor tissue due to the abnormal vascularization. Further, dosing schemes are crucial since the tumor response depends not only on the dynamics of the agents and the fluids that carry them but also on the complex physiology of the body systems and the local tumor tissue. Recent theoretical studies with the aid of mathematical modeling and computational simu-

lation, coupled with the latest experimental technologies (e.g., intravital microscopy), have highlighted the complexity of chemotherapy delivery and uptake in live tumors [van de Ven *et al.*, 2012, van de Ven *et al.*, 2013].

Theoretical modeling of chemotherapy usually relies on partial differential equation (PDEs) to describe the transport dynamics as well as the pharmacokinetics of therapeutic agents in time and space. Beginning with the vasculature, most studies have focused on the interaction between the vascular structure and blood flow, which contributes to the transport characteristics and agent availability through the vascular network as a closed system (e.g., [McDougall *et al.*, 2002, Stephanou *et al.*, 2005, McDougall *et al.*, 2006, Bartha & Rieger, 2006, Lee *et al.*, 2006, Welter *et al.*, 2008, Welter *et al.*, 2009, Welter *et al.*, 2010]). However, fluids and substrates are exchanged through the vascular wall in the capillary regions. In the tumor interstitium, transport subject to interstitial fluid flow (IFF) has been investigated, where barriers due to lymphatic dysfunction as well as other common tumor pathologies (e.g., elevated vascular hydraulic conductivity and resultant attenuated transvascular osmotic pressure) were studied theoretically by Baxter and Jain [Baxter & Jain, 1989, Baxter & Jain, 1990]. These authors modeled the source of fluids and substrates through a vascular continuum and the effect of vascular flow was not considered. Recently, IFP, IFF and vascularized tumor growth were coupled dynamically in computational models by [Cai *et al.*, 2011, Wu *et al.*, 2013, Welter & Rieger, 2013].

Pharmacokinetics and pharmacodynamics (PKPD) models, which combine reaction-diffusion PDEs that model the transport of chemotherapy agents in the tissue, and mass-action ordinary differential equations (ODEs) that model biochemical reactions in the cells, have been used to predict the tumor response to certain types of drug molecules (e.g., doxorubicin and cisplatin, see [Jackson, 2003, Sanga *et al.*, 2006, Sinek *et al.*, 2009]), or to predict agent availability due to innovative transport modalities (e.g., nanoparticles or macrophages loaded with nanoparticles, see [Sinek *et al.*, 2004, Owen *et al.*, 2004], respectively), as well as the resulting tumor response and therapy limitations ([Frieboes *et al.*, 2009, Sinek *et al.*, 2009]). Although most of these efforts are tied to angiogenesis models as the source of the agents, the extravasation is often assumed to be affected only by the transvascular concentration difference and the physical pressure from tumor cells outside the vasculature. The effects of convective transport by the interstitial fluid are usually not considered or are coupled with the tumor cell velocity (e.g., [Jackson, 2003]) instead of the IFF which can carry the agents through the interstitium.

Very recently, interstitial fluid flow and drug delivery have been investigated by [Welter & Rieger, 2013] in a 3-dimensional vascular tumor growth model using a continuum model for tumor cells and an arteriole-venous vascular network that accounted for drainage of interstitial fluid due to lymphatic function. [Welter & Rieger, 2013] found

that the IFP, the IFF and the drug distributions are strongly heterogeneous due to the vascular architecture.

Here, we study the transport of therapeutic agents in a 2-dimensional interstitial continuum covered by a discrete tumor vasculature initially laid out as a rectangular grid to simulate the pre-existing capillary network. Unlike [Welter & Rieger, 2013] where the arterio-venous system is explicitly built, the capillaries considered here serve as both arterial and venous conduits since they are the smallest blood-carrying units in the tissue. Our approach builds on the tumor growth model developed in [Macklin *et al.*, 2009, Wu *et al.*, 2013], where we investigated the transcapillary and interstitial fluid dynamics during vascularized tumor growth coupled with the effect of blood and lymphatic vessel collapse. In particular, we investigated the effect of tumor vascular pathologies on the fluid flow across the tumor capillary bed, the lymphatic drainage and the IFP. Here, we focus on how the pathologies affect the transport of therapeutic agents during chemotherapy and the response of the tumor through the fluid flow. Considering the concentration of chemotherapy agents both in the vasculature and in the interstitium linked by the transcapillary fluid flux (modeled in [Wu *et al.*, 2013]), as well as the loss of agents into the lymphatic system through the lymphatic fluid drainage (modeled in [Wu *et al.*, 2013]), the model presented here can adapt to diverse delivery scenarios according to the specific agent characteristics and delivery protocols. In particular, we apply the model to study two injection schemes. The first, called "bolus injection," applies to agents injected upstream of the tumor vasculature for a short period of time (e.g., 1- 10 min). The second scheme, called "constant injection," applies to agents injected upstream for a prolonged period of time (~ 100 minutes). We study the temporal and spatial distribution of agents in the vasculature and the interstitium together with the transcapillary concentration flux. We evaluate the efficiency of agent delivery while varying the functional lymphatic distribution and associated pathological factors. Finally, we assess the effects of chemotherapy on a growing tumor.

The outline of the paper is as follows. We present the mathematical models in Sec. 2, and describe the numerical details in Sec. 3. We present the results in Sec. 4, followed by a discussion in Sec. 5, in which the conclusion and future work are also described.

2 The coupled mathematical model

We review the agent transport model that is applied to the vascular tumor growth model described in [Wu *et al.*, 2013]. For completeness, the modeling of vascular and interstitial fluid dynamics from [Wu *et al.*, 2013] is briefly described in Sec. 2.1. In Sec. 2.2 we consider the tumor progression under the influence of therapeutic agents where we describe the agent transport in the vasculature and in the interstitium by two

reaction-convection-diffusion equations coupled by the transcapillary flux (Sec. 2.3).

2.1 Vascular and interstitial fluid dynamics

Following [Wu *et al.*, 2013], we define the vasculature on a Cartesian grid. A vessel node is the basic unit located at a grid point and the vasculature configuration is given by the connection between neighboring nodes. Responding to the TAF released by the hypoxic cells in the tumor interior, endothelial cell sprouts are generated, grow and fuse to expand the vascular network. We describe the pre-existing vasculature on this grid-like network in which sprouts can be generated from and fuse into, analogous to [McDougall *et al.*, 2002, Stephanou *et al.*, 2005, McDougall *et al.*, 2006, Bartha & Rieger, 2006, Lee *et al.*, 2006, Welter *et al.*, 2008, Welter *et al.*, 2009, Welter *et al.*, 2010]. During angiogenesis, the sprouting pattern along stimulated vessels can be mediated by Notch-Delta signaling between adjacent endothelial cells (ECs) that ensures no adjacent ECs sprout simultaneously under the TAF stimulation [Hellstrom *et al.*, 2007, Jakobsson *et al.*, 2009]. We incorporate this sprouting pattern analogously to [Welter *et al.*, 2009] (investigated in detail in [Bentley *et al.*, 2008]). After sprouts are generated, they advance stochastically in space according to TAF and ECM gradients as in [McDougall *et al.*, 2002, McDougall *et al.*, 2006, Macklin *et al.*, 2009]. In the developing capillary network, blood begins to flow and the blood vessel pressure and flow are computed along the vessels (Sec.2.1.1) together with interstitial fluid coupled by transcapillary fluid flux (Sec.2.1.2). Lymphatic drainage is also included in the dynamics of the interstitial fluid, described in Sec.2.1.4. In [Wu *et al.*, 2013], the vessel radius is adapted to the local vessel pressure, shear rate and metabolite levels in the tumor growth model, following [Pries *et al.*, 1998] and as described in the Appendix A.

2.1.1 Blood flow

We model the blood flow by a generalized Poiseuille's law [Fung, 1997]

$$Q_{qp} = \frac{\pi R_{qp}^4 (P_{v_q} - P_{v_p})}{8\mu_{apparent}L},$$
(1)

where Q_{qp} stands for the blood flow from a vessel node q to a neighboring node p, and P_{v_q} and P_{v_p} are the corresponding blood pressures. R_{qp} is the radius of the vessel segment from q to p, and $\mu_{apparent}$ is the apparent plasma viscosity.

The net blood flow flux passing through each vessel node p from all the neighboring nodes is governed by:

$$\sum_q Q_{qp} = O_V.$$
(2)

which by using Eq. (1) results in a system of equations for blood pressure P_v at the vessel nodes.

2.1.2 The transcapillary fluid flux (TFF)

We model the TFF by Starling's law [Fung, 1997]

$$O_V = K_{Vf} S_V (P_v - P_f - \omega(\pi_v - \pi_i)), \tag{3}$$

where K_{Vf} is the vascular hydraulic conductivity, differing between the host and tumor tissues (see Table 1) in pathological cases while being equal in the normal base case, and $S_V = \sum_{neighbour} \pi R_n L_n$ is the summation of half vessel segment surface area connecting to the neighbouring vessel nodes (The surface area of other half goes to the neighbouring node). P_v is the blood pressure and P_f is the IFP on the opposite side of the vascular wall. Further, ω is the average osmotic reflection coefficient for plasma proteins, while π_v and π_i are the osmotic pressures of the plasma and interstitial fluid, respectively. In the following, we name $P_e = P_v - \omega(\pi_v - \pi_i)$ to be the effective pressure which quantifies the value that competes with P_f. Notice P_v, P_f and P_e are all in the unit of Pa.s. Rescaling O_V by the characteristic volume V_T in the interstitial continuum we obtain the exchange rate (the volume in the continuum is coincident with the vessel segment $V_T = L^3$, where L is the characteristic length; hence, V_T is fixed and is assumed for simplicity to be unaffected by the vasculature volume):

$$J_V = \frac{O_V}{V_T} \tag{4}$$

which is the source term in Eq.(6) below describing the IFP.

2.1.3 Interstitial fluid pressure (IFP) and velocity (IFF)

Following [Wu $et\ al.$, 2013], we use Darcy's law to relate the IFP and IFF:

$$\mathbf{v_f} = -K \nabla P_f \tag{5}$$

where K is the interstitial hydraulic conductivity. Conservation of mass then yields

$$\nabla \cdot (\phi_f \mathbf{v_f}) = \phi_f (J_V - J_L) - \nabla \cdot (\phi_c \mathbf{v_c}). \tag{6}$$

where ϕ_f and ϕ_c are the water and cell volume fractions, respectively, $\mathbf{v_c}$ is the cell velocity (Sec. 2.2) and J_L is the lymphatic drainage (Sec.2.1.4). The physical units are compatible because in Eq. (4), the units of the transvascular fluid flux O_v are volume/time divided by the characteristic volume V_T. The exchange rate is then a rate with units of 1/time, matching the source term in the continuum Eq. (6). Since we solve for the blood pressure and interstitial pressure together by the iterative method,

the convergence of the two variables ensures the mass balance between the two systems via the transvascular fluid flux. Note that the 2nd term on the right-hand side of Eq. (6) describes the flux of water due to cell division (uptake of water) as well as cell death (source of water). We assume comparable densities of water and cells, where ϕ_f and ϕ_c are considered as constants ($\phi_c = \phi_f = 0.5$), following [Wu *et al.*, 2013].

2.1.4 Lymphatic drainage

The lymphatic drainage is modeled as:

$$J_L = \lambda_{fL} c(P_c, L)(P_f - P_L) \cdot 1_{P_f > P_L} \tag{7}$$

where $c(P_c, L)$ is the lymphatic drainage capacity, λ_{fL}, a constant rate and P_L is the critical IFP level below which there is no drainage. $1_{P_f > P_L}$ is 0 for $P_f \leq P_L$ [Scallan *et al.*, 2010] and 1 for $P_f > P_L$. The function $c(P_c, L)$ depends on the tumor hydrostatic pressure P_c and the lymphatic vessel density L:

$$c(P_c, L) = \begin{cases} (1 + \frac{Lymmax - 1}{KLmin} P_c)L & P_c \leq KL_{min} \\ Lymmax(1 - \frac{P_c - KL_{min}}{KL_{max} - KL_{min}})L & KL_{min} < P_c \leq KL_{max} \\ 0 & P_c > KL_{max} \end{cases} \tag{8}$$

For small hydrostatic pressures P_c below a partial collapse threshold KL_{min}, $c(P_c, L)$ increases with P_c and the drainage increases as hydrostatic pressure from the cells pushes fluid into the lymphatic vessels ($Lymmax$ at the maximum). When the pressure increases beyond KL_{min}, the lymphatic vessels responding to the pressure P_c begin to partially close, and $c(P_c, L)$ subsequently decreases, eventually reaching 0 at KL_{max} as the lymphatic vessels collapse. We assume that the continuum lymphatic vessel field is degraded by matrix degrading enzymes M (described in Appendix B) at a rate λ_{ML}; hence,

$$\frac{dL}{dt} = -\lambda_{ML} M L. \tag{9}$$

P_c is described in Sec.2.2. In the following we refer to KL_{max} as the lymphatic resistance to represent the strength of the lymphatic vessel wall that is subjected to physical forces (i.e., hydrostatic pressure). The distribution of functional lymphatic vessels is affected by M in time and by P_c in space. Since we do not consider lymphangiogenesis in this work, the loss of functional lymphatic vessels due to M cannot be recovered. However, the function of lymphatic vessels can be partially recovered by decreasing P_c. We note that in [Welter & Rieger, 2013], the amount of functional lymphatics is introduced as a free parameter and different ratios between tumor and normal lymphatic distributions are investigated for a static tumor. Here, if P_c is greater than KL_{max}, then the lymph vessels are assumed to collapse and cannot drain any fluid regardless of the IFP.

2.2   Tumor mechanics and chemotherapy

Following [Macklin *et al.*, 2009, Wu *et al.*, 2013] and references therein, we assume cellular motion within the ECM as an incompressible fluid flow in a porous medium; thus, the cell velocity is proportional to the forces following Darcy's law. We model all solid phases moving with a single cellular velocity field. Accordingly, the velocity is given by:

$$\mathbf{v}_c = - \overbrace{\mu \nabla P_c}^{\text{pressure gradient by mitosis}} + \underbrace{\chi_E \nabla E}_{\text{haptotaxis}} \tag{10}$$

where μ is the cell-mobility modeling the net effects of cell-cell and cell-matrix adhesion, E is the ECM density (composed of non-diffusible matrix macromolecules such as fibronectin, collagen, and laminin) and χ_E is the haptotaxis coefficient. See Appendix B for the details of E. Details regarding μ and χ_E can be found in the Appendix in [Wu *et al.*, 2013]. We associate the growth and death of tumor cells with the rate of volume change by assuming that the tumor cell density is constant in the proliferating region:

$$\nabla \cdot \mathbf{v}_c = \lambda_p \tag{11}$$

where λ_p is the net proliferation/death rate. Note that proliferating cells uptake water while dying cells release water. The pressure satisfies:

$$-\nabla \cdot (\mu \nabla P_c) = \lambda_p - \nabla \cdot (\chi_E \nabla E) \tag{12}$$

We assume that in the proliferating region, the cell mitosis/death rate is proportional to the amount of nutrient present and that apoptosis may occur. We also assume that volume loss may occur in the necrotic region and that there is neither proliferation nor apoptosis in either the host or hypoxic tissue regions.

We include the effect of the agent (drug) into the net proliferation/death rate in the tumor region Ω :

$$\lambda_p(\sigma) = \begin{cases} 0 & \text{outside } \Omega \\ \lambda_M \sigma (1 - \overbrace{\lambda_{effect} D}^{\text{pharmacodynamics}}) - \lambda_A & \text{in } \Omega_P \\ 0 & \text{in } \Omega_H \\ -G_N & \text{in } \Omega_N \end{cases} \tag{13}$$

where λ_M is the mitosis rate, σ is the oxygen concentration (that is given in Eq. (15) below), and λ_A is the apoptosis rate. Further, λ_{effect} is the rate of drug-induced cell death, which represents a simple pharmacodynamic model. When $\lambda_{effect} D \leq 1$, the net

proliferation is reduced. When $\lambda_{effect}D > 1$, cell death is introduced and contributes to tumor shrinkage. Note that the drug acts only on the proliferating cells in Ω_P, and not on the hypoxic cells in Ω_H or the necrotic cells in Ω_N. The parameter G_N is the rate of volume loss in the necrotic core, which is taken to be constant (e.g., [Macklin *et al.*, 2009, Wu *et al.*, 2013]).

Following [Wu *et al.*, 2013], we model the transport of oxygen by a quasi-steady reaction-diffusion equation:

$$0 = \nabla \cdot (D_\sigma \nabla \sigma) - \lambda^\sigma(\sigma)\sigma + \lambda^\sigma_{vasc}(\mathbf{x}, t, 1_{vessel}, P_f, \sigma, h) \qquad (14)$$

where the oxygen is supplied by the vasculature (both pre-existing and neo-vasculature) at a rate λ^σ_{vasc}, diffuses with coefficient D_σ, is uptaken by normal cells with rate λ_{host}, by proliferating cells with rate λ_σ, by hypoxic cells with rate λ_{hyp}, and degrades with rate λ_{nec} in the necrotic core:

$$\lambda^\sigma = \begin{cases} \lambda^\sigma_{host} & \text{outside } \Omega, \\ \lambda^\sigma_{prolif} & \text{in } \Omega_P, \\ \lambda^\sigma_{hyp} & \text{in } \Omega_H, \\ \lambda^\sigma_{nec} & \text{in } \Omega_N. \end{cases} \qquad (15)$$

In particular, the oxygen released by the vascular network is modeled as:

$$\lambda^\sigma_{vasc} = \overline{\lambda}^\sigma_{vasc} \mathbf{1}_{vessel}(\mathbf{x}, t)(\frac{h}{\overline{H}_D} - \overline{h}_{min})^+(1 - k_{P_f}\frac{P_f}{P_e})(1 - \sigma), \qquad (16)$$

where $\overline{\lambda}^\sigma_{vasc}$ is the transfer rate, $\mathbf{1}_{vessel}$ denotes the characteristic function of the vascular network (e.g., 1 at the locations of the vessels and otherwise 0), h is the hematocrit in the blood, $\overline{H}_D$ is the normal value of hematocrit in the blood and $\overline{h}_{min}$ is the minimum hematocrit needed to extravasate oxygen. The extravasation occurs only when $\frac{h}{\overline{H}_D} - \overline{h}_{min} > 0$, which we denote by $+$. Note that we have not differentiated the effects of convection-induced extravasation and diffusion-induced extravasation of oxygen due to the lack of information of the involved parameters given that oxygen is quite different from large molecules and therapeutic agents. Due to the lipid-solubility of oxygen, the entire capillary wall is available for oxygen to diffuse through, which makes oxygen transvascular diffusion less dependent on the pore size of the capillary (permeability) [Pittman, 2011] compared to water-soluble molecules (i.e., glucose) and large particles (i.e., drug agents). Moreover, the dependence of transvascular fluid convection for oxygen and drugs are also different. In addition, it was reported that regions where there are small differences between the blood pressure and IFP tend to be associated with tumor cell hypoxia and decreasing the IFP reduces the hypoxia [Jain, 2005], though there is no direct evidence of the effect of IFP on oxygen extravasation. Based on this observation, we add a phenomenological constraint on oxygen extravasation through the

term $(1 - k_{P_f}\frac{P_f}{P_e})$ where k_{P_f} evaluates the impact of the ratio $\frac{P_f}{P_e}$ on the overall oxygen extravasation of each vessel.

2.3   Pharmacokinetics Model

We describe the dynamics of the agent concentration in the vasculature (F) and in the interstitium (D), which are coupled through the transvascular agent flux O_{F_p}.

We derive the model as a function of the vasculature by imposing mass conservation at the vessel nodes. For each vessel node p over a time interval Δt, the agent level F_p in the bloodstream obeys:

$$\frac{dF_p}{dt} = (\sum_u Q_{up}(F_u - F_p) - O_{F_p})/V_p - r \tag{17}$$

where the transvascular agent flux O_{F_p} is modeled as

$$O_{F_p} = \left\{ \begin{array}{ll} (1 - k_O)F_pO_{V_p} & O_{V_p} \geq 0 \\ (1 - k_O)DO_{V_p} & O_{V_p} < 0 \end{array} \right. + k_DS_pF_p - k_TS_pD \tag{18}$$

In Eq. (17), the u's represent the upstream neighbor nodes and Q_{up}'s are the blood flow from nodes u's to node p. Further, $V_p = \sum_u \pi R_{up}^2 L_{up}$ is the vascular volume from all upstream u's to p, where R_{up} and L_{up} are the radius and length of the cylinder segments and r is a reaction term that accounts for the interaction between nanoparticles and vessel walls [Decuzzi *et al.*, 2009, Frieboes *et al.*, 2013]. For example, $r = r_pF_p$ where r_p is a function of the wall shear stress and the affinity between the vessel wall and the specific nanoparticle, independent of the concentration F_p. In this paper, the agent is assumed not to adhere on the vessel wall thus $r_p = 0$, however, we present the model as general as possible for future references.   In Eq. (18), k_O is the agent osmotic reflection coefficient, which is affected by the agent size as well as the size and surface area of the vessel wall pores. O_{V_p} is the total TFF from the upstream neighbor nodes u's to p according to Eq. (3). When O_{V_p} is negative, TFF convects the agent from the interstitium to the blood. The parameters $k_D = \overline{K}_DS_p$ and $k_T = \overline{K}_TS_p$ are the transfer rates across the wall from the blood to the tissue and from the tissue to the blood by other transport components, respectively, including diffusion [Jain & Stylianopoulos, 2010]. $\overline{K}_T$ and $\overline{K}_D$ can be associated with vascular hydraulic conductivity K_{Vf}. $S_p = \sum_u 2\pi R_uL_u$ is the vascular surface area from all upstream u's to p. Notice as long as the reaction term r linearly depends on F_p (i.e., as in [Decuzzi *et al.*, 2009, Frieboes *et al.*, 2013]), the sign of F_p is preserved. Even in the most extreme washout scenario where there is no agent source from either the upstream blood supply or the interstitium, and the transvascular fluid flux $O_{V_p} \geq 0$, F_p decays

exponentially as $e^{-t(\sum_u Q_{up}+(1-k_O)O_{V_p}+k_D S_p+r_p)}$ and approaches 0 asymptotically from above.

For the agent concentration D in the intersitium, we account for the agent exchange from the vessel (at rate J_{F_p}) and the agent loss through drainage into the lymph system (at a rate J_{DL}), as well as convection, diffusion, uptake by cells and natural decay of the agents. Accordingly, we arrive at the advection reaction diffusion equation

$$\frac{\partial D}{\partial t} + \tau_F \overbrace{\nabla \cdot (D\mathbf{v}_f)}^{\text{convection}} = \overbrace{D_D \Delta D}^{\text{diffusion}} + J_{F_p} \cdot 1_{vessel} - J_{DL} - (\lambda_{decay} + \lambda_{uptake} \cdot 1_{tumor})D \quad (19)$$

where $\mathbf{v_f}$ is the interstitial fluid velocity (e.g., from Eq.(5)) and D_D is the diffusion coefficient, which differs between the host and tumor tissues (see Table 1). The parameter λ_{uptake} is the agent uptake rate by tumor cells and λ_{decay} is the natural decay rate. The parameter τ_F in front of the convection term is known as the retardation factor in the interstitium and is for simplicity here taken to be 1 (Table 1). 1_{vessel} is 1 within vessels where the effective pressure is greater than the IFP, while 1_{tumor} is 1 in regions of live tumor tissue. Finally, the vessel-tissue exchange flux J_{F_p} and the drainage flux J_{DL} are given by:

$$J_{F_p} = \frac{O_{F_p}}{V_T} \quad (20)$$

and

$$J_{DL} = DJ_L. \quad (21)$$

3 Numerical details

Briefly, following [Wu *et al.*, 2013] we discretize the elliptic/parabolic equations Eqs. (10), (6) and (19) in space using centered finite difference approximations and the backward Euler time-stepping algorithm. The discrete equations are solved using a nonlinear adaptive Gauss-Seidel iterative method (NAGSI)[Macklin & Lowengrub, 2007, Macklin & Lowengrub, 2008]. We use a first order upwind discretization of the advection term explicitly in time. The time step $\Delta\tau$ is chosen to satisfy the CFL condition in both the vasculature and the tissue: $\Delta\tau \leq min(\frac{V_{qp}}{Q_{qp}}, \frac{\Delta x}{|v_{i,x}|+|v_{i,y}|})$ where $|v_{i,x}|$ and $|v_{i,y}|$ are the magnitudes of the velocity in the $x-$ and $y-$, respectively.

4 Simulation and Parameter studies

We first consider two representative injection schemes and evaluate the agent delivery under varying conditions in Sec. 4.1. We show the effect of pathological factors on the agent distribution and delivery characteristics in Sec. 4.2. We simulate chemotherapy and discuss the effect of pathological factors on tumor response in Sec. 4.3. The parameters used in these studies are given in Table 1.

As described in our previous work [Wu *et al.*, 2013], a uniform pre-existing vascular network arranged on a Cartesian grid in a 2×2 mm^2 area is used to represent the tissue space in which the simulations are performed (Figs. 1 and 2)). A pressure gradient is imposed on the domain boundary, 3750 Pa.s at the lower left and 3000 Pa.s at the upper right, linearly decreasing between the two corners. This defines the 16 vessel nodes along the left and bottom boundaries as inlets while the 16 vessel nodes along the right and top boundaries are outlets. As in[Wu *et al.*, 2013], the model is calibrated such that the vasculature provides sufficient oxygen ($\sigma = 0.76 \sim 1$) to support normal tissue metabolism [Intaglietta *et al.*, 1996]. A small avascular tumor nodule is placed in the center of the domain to initialize the simulations. The oxygen level in the tumor tissue is lower than the surrounding tissue because the tumor is assumed to uptake more oxygen delivered by the vasculature. As the tumor grows, the oxygen concentration within the tumor decreases further and cells therein become hypoxic (blue) and necrotic (brown), see Figs. (6 and 7).

4.1 Delivery of agents in the vascular-interstitial space

We simulate chemotherapeutic agent delivery by either constant or bolus injection, i.e., we either inject agents through the end of the simulation (100 min.) or inject agents instantaneously upstream of the tumor vasculature, with agents passing through the vascular wall solely by convection. Following [Baxter & Jain, 1989] and references therein, the value of the diffusive component of transcapillary flux for molecules (e.g., monoclonal antibodies) has been estimated to be 0-10%; here, we focus on large molecules and particles, and assume $k_T = k_D = 0$ in Eq.(18). We investigate the temporal and spatial distribution of agents in the vasculature and interstitium simultaneously together with the transcapillary agent concentration flux.

We first simulate a constant injection scheme. Agents are injected continuously from 16 inlets located along the top and left boundaries of the tissue region (see $t = 0.17$ min. in Fig. 1). At ≈ 1 min. the agents in the blood reach the tumor region (see Row 2 in Fig. 1). At 2.5 min, the agents in the vessels cover almost the entire region, but the agent extravasation is low due to the large P_f in the tumor which impedes TFF (Column 2, Row 3 in Fig.1). After ≈ 4 min., the agent concentration in the blood reaches a steady condition in which the upstream is at a higher concentration (close to the concentration from the inlets) while the downstream maintains a lower concentration due to the extravasation into the tumor tissue (Row 1 in Fig. 2). At ≈ 16 min. (Row 2 in Fig. 2), the concentration in the tissue remains continuously elevated due to the flux from the vessels while still showing a nadir in the tumor region due to the lack of TFF, which is more pronounced later at time 100 min. (Row 3 in Fig. 2).

In the case of bolus injection, the agents also reach the tumor vasculature at ≈ 1

min. At $t = 2.5$ min, the bulk of the injected agents passes through the tumor and enters the washout phase. Interestingly, the agent is confined to the tissue even after $t = 100$ min. due to the inability to travel back to the bloodstream during washout as well as the lack of tumor lymphatic drainage. The blue curve in Fig. 3 shows a cross-sectional view of the agent distribution in the tissue at $t = 100$ min. For comparison, the red curve shows the behavior of agents that can bi-directionally pass through the vascular wall ($k_T = k_D > 0$).

4.2 Effect of vascular pathology on agent delivery

As discussed in [Wu *et al.*, 2013], tumor vascular pathologies play a critical role in elevating and maintaining IFP as well as the outward tumor fluid flow, resulting in physical transport barriers that hinder agent delivery. Here, we illustrate the delivery of agents taking into consideration lymphatic and vascular pathologies such as elevated vascular/interstitial hydraulic conductivites and attenuated transvascular osmotic pressure differences. We first quantify the average agent concentration in the tumor versus time under each pathology combined with different lymphatic resistances KL_{max} for both instant bolus and constant injection schemes. In all cases, a larger lymphatic resistance (i.e., $KL_{max} = 3$, blue curves in Fig. 4) contributes to more rapid delivery to the tissue. However, this also leads to a trade-off later in the bolus injection scheme (Column 1 in Fig.4), where a larger lymphatic resistance contributes to a more rapid washout while tumors with smaller lymphatic resistance behave as a reservoir of agents for the surrounding tissue (Red curves in column 1 in Fig. 4). Interestingly, these behaviors are accentuated with elevated vascular hydraulic conductivity (Row 2 in Fig. 4). Transport with elevated interstitial hydraulic conductivity and attenuated transvascular osmotic pressure difference behaves similarly in terms of the average concentration in the tumor (data not shown).

In Fig.5 we quantify the agent availability in the tumor over time (AUC) after the same bolus injection under the variation of KL_{max} and with elevated vascular/interstitial hydraulic conductivity. We find that the AUC increases with KL_{max} for all cases, while elevated vascular hydraulic conductivity contributes to higher AUC and elevated interstitial hydraulic conductivity contributes to lower AUC (Fig.5, left).

We further evaluate the AUC with a permeable agent that can move freely through the vascular wall without TFF ($k_D = k_T > 0$, Fig. 5, right). The AUC in all three cases is elevated. However, the AUC decreases as KL_{max} increases, while cases with elevated vascular/interstitial hydraulic conductivities exhibit a lower AUC. With elevated interstitial hydraulic conductivity, the AUC is low both when $k_D = k_T = 0$ and $k_D = k_T > 0$, which is an issue for transport in general. On the other hand, an elevated vascular hydraulic conductivity contributes to a higher AUC when the agents depend solely on

TFF for transport, while with additional transvascular transport the elevated vascular hydraulic conductivity contributes to a lower AUC. This suggests that increasing the ability of the agents to move through the vascular wall may not necessarily increase the net agent accumulation in the tissue when such vascular pathologies are present. Similar investigations have recently been performed in [Welter & Rieger, 2013]. This is described further in the Discussion.

4.3 Chemotherapy

In order to further investigate the interactions of agent delivery with heterogenous tumor dynamics during treatment, we simulate chemotherapy assuming constant injection of macromolecule drugs for 5 days, with $k_D = k_T = 0$ and with elevated tumor vascular/interstitial hydraulic conductivities. In this case, the drug is uptaken by tumor cells in contrast to the free agent in Sec. 4.1 and Sec. 4.2. Fig.6 shows the drug distribution at day ≈ 18 before the tumor responds to the drug. Consistent with [Wu et $al.$, 2013], the IFP with elevated tumor interstitial hydraulic conductivity provides a broad-base plateau profile where the IFP is nearly constant in the tumor interior (Column 2). This profile contributes to a larger area with high IFP and fluid flow away from the tumor [Wu et $al.$, 2013]. This decreases the drug concentration in and near the tumor (Column 2), while the plateau profile itself smoothes the drug distribution inside the tumor (Column 2).

The IFP with elevated tumor vascular hydraulic conductivity (Column 3) is larger than that of control (Column 1) due to excessive fluid extravasation. The excessive fluid extravasation when the vascular hydraulic conductivity is elevated contributes to higher drug extravasation, thus increasing the concentration in the interstitium (Column 3). However, the distribution is more heterogeneous compared to the base case– there is a larger disparity between the drug concentrations in the tumor interior and in the tumor periphery, which may contribute to a decreasing rate of tumor shrinkage (discussed further below). The same observation is also found in [Welter & Rieger, 2013], in which the macromolecules are distributed around the tumor perimeter. In their studies, however, the drug distribution is even more heterogeneous (see Discussion).

During the simulation, the treated tumor responds to the drug by either decreasing its rate of growth or decreasing its size (compared to untreated tumors). Fig. 7 shows snapshots of tumor pressure, tumor tissue, vasculature during therapy from day ≈ 18 to the end of the treatment (day ≈ 23). The vascular/interstitial hydraulic conductivities are elevated. At day ≈ 18, although all the treated tumors experience negative pressure due to cell death and lysing, those with elevated interstitial hydraulic conductivity maintain a higher pressure due to lower drug concentration in the interior (Column 2 in Fig. 6). However, tumors with elevated vascular hydraulic conductivity experience the

most negative pressure due to an increased drug concentration in the tissue caused by excessive fluid extravasation. Correspondingly, after ≈ 5 days, (at day ≈ 23) the tumor with elevated vascular hydraulic conductivity shrinks the most, while the tumor with elevated interstitial hydraulic conductivity shrinks the least.

We quantify the tumor radius after ≈ 5 days of treatment (Fig. 8) by varying the strength λ_{effect} from 0 to 1 in increments of 0.2, where 0 corresponds to an untreated tumor. The cases with elevated vascular and interstitial hydraulic conductivities are shown in green and blue, respectively; their combination is shown in cyan, and their further combination with attenuated transvascular osmotic pressure difference is plotted in magenta. A tumor with none of these vascular pathologies is considered to be the control and shown in red. The black horizontal line corresponds to the tumor radius before therapy. Untreated tumors with elevated interstitial hydraulic conductivity grow faster and those with elevated vascular hydraulic conductivity grow slower due to the inhibitory effects of IFP on oxygen extravasation from Eq.(16). On the other hand, these tumors do not shrink until the drug strength increases to ~ 0.9, which is a slightly slower effect than shown the control (~ 0.85) due to the excessive fluid flow from the tumor into the surrounding tissue. In contrast, untreated tumors with elevated vascular hydraulic conductivities (green, magenta, and cyan) grow slower compared to both the control and to tumors with elevated interstitial hydraulic conductivities. This is due to lower oxygen extravasation as a result of IFP hypertension. These tumors begin to shrink when the drug concentration increases to ~ 0.45. However, with elevated vascular hydraulic conductivity alone, the shrinkage seems to saturate (green line) as the drug concentration increases (note the transition between the green curve and the cyan or magenta curves) due to the heterogeneity and low drug concentration in the tumor interior. The tumor shrinkage slows down once it reaches a radius $\lesssim 0.35$ mm.

5 Discussion

In this study we employed mathematical modeling and simulation to quantitatively evaluate the role of hypertensive IFP and associated pathological conditions on the delivery of chemotherapeutic agents to vascularized tumors and on the tumor response to these agents. We found that agent extravasation from the bloodstream is hindered by the hypertensive IFP through convection by the transvascular fluid flux. While the agents can be washed away from the tumor into the neighboring host tissue as a result of high IFF near the tumor border, inside the tumor, however, the agents can be confined to the interstitium due to the lack of lymphatic function contributing to a relatively low and homogeneous IFF in the tumor interior. These findings are consistent with pioneering work in [Baxter & Jain, 1989], in which transport in the interstitium was modeled with a continuum vascular source without blood flow and lymphatic drainage. In their work,

there is strictly no back flow of IFF into the vasculature due to the continuity of the modeled vasculature. Here, modeling a discrete vasculature, slight back flow of IFF can be found with large vascular hydraulic conductivity (data not shown) near neighboring but unconnected vessels with a large pressure difference between them. This does not contribute to a considerable amount of agents draining back into the circulation. We further analyzed the contribution of the lymphatic function as well as those of tumor vascular pathologies to impaired agent delivery. In a time scale of hours, tumors with more functional (i.e., normal) lymphatics increase agent concentration more rapidly, but they also experience quicker washout under bolus injection. This finding has recently been observed experimentally [van de Ven *et al.*, 2013].

We investigated agent availability in the tumor over a longer period of 100 min. using agents with/without additional transvascular transport (agents with/without significant transvascular diffusivity). The AUC increases as lymphatic resistance increases with less permeable agents while the AUC decreases with permeable agents. With elevated interstitial hydraulic conductivity, the AUC is low in general regardless of the agent transvascular transport capability. Interestingly, an elevated vascular hydraulic conductivity contributes to the highest AUC when the agent is less permeable, while presenting lower AUC when the agent is more permeable. Both elevated vascular hydraulic conductivity and lymphatic resistance correspond to higher fluid extravasation and thus higher fluid drainage by the lymphatics (see Fig. 21 in [Wu *et al.*, 2013]). When the transport depends more on the transvascular convection, the positive correlation of the AUC with vascular hydraulic conductivity or lymphatic resistance is clear, which is also observed in [Welter & Rieger, 2013], where a drug with moderate permeability is studied. On the other extreme is the case where the drug extravasation depends so much on the additional transport (i.e., large transvascular diffusivity) that the extravasation loses sensitivity to increases of transvascular fluid due to increases in lymphatic resistance. In this case, more fluid extravasation is actually a disadvantage rather than an advantage to maintain a high level of agent concentration in the interstitium, since more fluid drainage ultimately results in more drug washout into the lymphatics. Therefore, either elevated vascular hydraulic conductivity or lymphatic resistance, which contributes to more fluid extravasation and thus more drainage, results in a reversed trend (descending vs. ascending) of AUC compared with the situation with only convection (see Fig. 5).

In recent work [Welter & Rieger, 2013] studied the effects of IFF and drug delivery on vascularized tumors using a 3-dimensional continuum tumor model. The sources of the IFF and the drug were supported by an arterio-venous vasculature that contains capillaries, large vessels (from circumferential growth) and arteriovenous shunts with a total pressure drop of about 12k Pa. In comparison, here we use a continuum model in 2-dimensions for tumor cells coupled with a cellular automaton model for the vasculature, and we consider an initial rectangular grid capillary network serving as both arterial

and venous conduits. In this study, the pressure drop is lower – only about 0.75k Pa (a typical pressure drop across the capillary bed is $\sim$ 2.7k Pa [Seeley *et al.*, 2004]). Correspondingly, the typical IFP in [Welter & Rieger, 2013] is about 6k Pa versus 2k Pa in this study. Further, we considered blood flow from 16 inlets arranged on a Cartesian mesh where the global blood pressure drop occurred primarily along the diagonal. As a result, the time scale of drug delivery in the blood is minutes in the present work vs. seconds in [Welter *et al.*, 2010]. Further, the spatial distributions of both the IFP and the IFF in [Welter & Rieger, 2013] are more heterogeneous than those observed here. The uneven IFP in [Welter & Rieger, 2013] arises due to locally abundant IFF inside the tumor. The distributions of the IFP and IFF obtained here are more consistent with the results in [Baxter & Jain, 1990]. Interestingly, the trends in the AUC predicted here and in [Welter & Rieger, 2013] are not exactly the same. We have observed two opposite behaviors of AUC as a function of the lymphatic resistance $KLmax$ in the transvascular convection case and the full transport case. For the former case, the AUC increases with lymphatic resistance, which is consistent with [Welter & Rieger, 2013]; however, when the full transport is considered, we have observed the reversed trend in AUC (as outlined above). We conjecture that in the work of [Welter & Rieger, 2013], where the fluid extravasation is abundantly supported by the arteriole-venous network with a large pressure drop, a decrease of AUC by increasing the lymphatic function would be observed when the transvascular diffusion is more dominant.

Interestingly, the average radial distribution in [Welter & Rieger, 2013] is consistent with our findings and both studies find large IFF within the tumor periphery and a layer of strong fluid drainage at the functional lymphatic front (tumor periphery in [Welter & Rieger, 2013]). Moreover, both studies show that an increase of lymphatic function promotes the overall IFF in the tumor micro-environment (see Fig.21 in [Wu *et al.*, 2013]). Similarly, despite different details of spatial distribution due to different vascular networks between [Welter & Rieger, 2013] and this work, both studies show that drug molecules distribute mostly along the tumor periphery, suggesting a general behavior transcending the details of the vascular network topologies.

Finally, we investigated the tumor response to chemotherapy during a 5 day period with the same vascularized tumor experiencing different vascular pathologies. We showed that tumors with elevated interstitial hydraulic conductivity grew the fastest without treatment or with lower drug dosages, consistent with our prediction in [Wu *et al.*, 2013]. As a result, these tumors have the most need for therapy and require higher dosages in order to shrink. We also showed that tumors with elevated vascular hydraulic conductivity have more hypoxic interiors, even though the oxygen concentration near the tumor boundary is elevated, due to constraints on oxygen extravasation in the presence of increased IFP in the tumor interior. The response of these tumors to the therapy slows down as the tumor shrinks due to the heterogeneity and low concentration of drug

in the tumor interior. We concluded that a normalization of the microevironment - both with respect to the vasculature and to the interstitium - is needed in order to optimize chemotherapy, whereas normalizing only one of these may not effectively overcome the physical resistance.

The insufficient delivery of therapeutic agents into tumors could be addressed by augmenting other transport components, such as transvascular diffusivity in a situation where the agent concentration is held high in the blood for a sufficiently long period of time. This could be achieved via nanoparticles that attach to the tumor vascular endothelium to serve as depots of drug into the surrounding tissue, as has recently been proposed by [Tasciotti *et al.*, 2008]. However, as the agent concentration in the blood decreases, the agent in the tumor would still wash out by the outward fluid flow and the bi-directional transport that lowers the agent retention by draining it back into the circulation (data not shown). This phenomenon is accentuated with elevated vascular/interstitial hydraulic conductivities. Moreover, the net concentration gain in the tumor by introducing an improved transvascular diffusivity decreases as lymphatic resistance increases (data not shown). However, under elevated vascular hydraulic conductivity the net gain is small, suggesting that the strategy of promoting tranvascular transport may not work well when the vascular hydraulic conductivity is elevated.

Normalization of the tumor vasculature [Jain, 2005, Jain *et al.*, 2007], e.g., decreasing the vascular hydraulic conductivity, is an emerging trend in tumor treatment in order to improve drug delivery into tumors. Here, we showed that an elevated vascular hydraulic conductivity during chemotherapy may contribute to a later stage physical resistance due to heterogeneity in the drug distribution and to low drug concentration in the tumor interior compared to the concentration at the tumor periphery, although the drug concentration in the tumor interior is actually larger than the base case with normal vascular/interstitial hydraulic conductivity. However, vasculature normalization by itself leaves the possibility of a stagnant tumor response due to an elevated interstitial hydraulic conductivity, in which a higher drug dose would be required to treat the tumor (Fig.8, blue curve) and could possibly lead to toxic side-effects. The results thus suggest that normalization of the extracellular matrix, which is related to the interstitial hydraulic conductivity [Levick, 1987], should be considered together with vascular normalization in order to achieve a better response.

Lastly, during chemotherapy, we did not consider the fluid production by tumor cell necrosis, which has the potential to further raise the IFP through cell lysis. This would require a biphasic model with balance laws between cell and water phases (see [Wise *et al.*, 2008, Frieboes *et al.*, 2010, Lowengrub *et al.*, 2010] and the references therein). This is the subject of future work.

6 Acknowledgements

A   Vessel radius adaptation

We summarize the vessel radius adaptation in [Wu *et al.*, 2013] which follows work by [Pries *et al.*, 1998, McDougall *et al.*, 2002, McDougall *et al.*, 2006, Macklin *et al.*, 2009]. The vessel radii are adapted in response to wall shear stress, intravascular pressure and hematocrit. The change in radius ΔR over a time unit is given by:

$$\Delta R = \left(S_{wss} + S_p + S_m - S_s\right) R \Delta t, \tag{22}$$

$$S_{wss} = \log\left(\tau_\omega + \tau_{ref}\right), \tag{23}$$

$$S_p = -k_p \log \tau_e(P_v), \tag{24}$$

$$S_m = k_m \log\left(\frac{Q_{ref}}{Q H_D} + 1\right), \tag{25}$$

where S_{wss} is the stimulus from wall shear stress τ_ω, and τ_{ref} is a constant included to avoid singular behavior at low shear rates. The wall shear stress τ_ω is calculated from [Pries *et al.*, 1998, Pries *et al.*, 1992]:

$$\tau_\omega = \frac{4\mu_{app}(R, H_D)}{\pi R^3} |Q| \tag{26}$$

where μ_{app} is apparent viscosity and can be computed as a function of vessel radius and hematocrit (see the previous references). The term $|Q|$ is the absolute value of the flow rate, as specified numerically in [Wu *et al.*, 2013]. Further, S_p is the stimulus by the intravascular pressure (considering only the vessel pressure) in the form of $\tau_e(P_v)$ from:

$$\tau_e(P_v) = 100 - 86 \cdot \exp\left[-5000 \cdot \left[\log\left(\log P_v\right)\right]^{5.4}\right], \tag{27}$$

where the values are obtained from [Pries *et al.*, 1998, McDougall *et al.*, 2002, McDougall *et al.*, 2006, Macklin *et al.*, 2009]. Finally, S_m is the stimulus from the flow carrying hematocrit, where Q_{ref} is a reference flow rate that is assumed to be larger than most of the flows in the network. The parameters k_p and k_m are the intensity coefficients.

B   Microenvironment interactions

In vascular tumor growth, the viable tumor cells and endothelial cells (ECs) remodel the extracellular matrix (ECM) by releasing matrix degrading enzyme (MDE). Here, we assume that the functional pre-existing lymphatics also degrade with MDE in Eq.(9) following previous work [Wu *et al.*, 2013]. The tumor microenvironment is described by introducing E representing the ECM and M representing MDE which are assumed to satisfy (following [Macklin *et al.*, 2009]):

$$\frac{\partial M}{\partial t} = \nabla \cdot (D_M \nabla M) + \bar{\lambda}^M_{prod}(1 - M)\mathbf{1}_{\Omega_V} - \bar{\lambda}^M_{decay}M + \bar{\lambda}^M_{spr.prod}\mathbf{1}_{sprouttips} \tag{28}$$

$$\frac{\partial E}{\partial t} = -\bar{\lambda}^E_{degradation}EM + \bar{\lambda}^E_{prod}(1 - E)\mathbf{1}_{\Omega_V} + \bar{\lambda}^E_{spr.prod}\mathbf{1}_{sprouttips} \tag{29}$$

where MDEs are produced by the viable tumor cells ($\Omega_V = \Omega_P \cup \Omega_H$) and neo-vascular sprouts with rates $\overline{\lambda}_{prod}^M$ and $\overline{\lambda}_{spr.prod}^M$, respectively. For simplicity, we assume MDEs are only released by the sprouting ECs, diffuse only with small D_M and decay with rate $\overline{\lambda}_{decay}^M$. We assume that the ECM is degraded by interacting with MDE with the rate $\overline{\lambda}_{degradation}^E$. However, the loss of MDE in this interaction is negligible compared to the MDE production, thus the term $-\overline{\lambda}_{degradation}^E EM$ only applies to the dynamics of ECM. The ECM can be further remodeled by the production by viable tumor cells and tip ECs with rates $\overline{\lambda}_{prod}^M$ and $\overline{\lambda}_{spr.prod}^M$, respectively.

References

[Bartha & Rieger, 2006] Bartha, K. & Rieger, H. 2006. Vascular network remodeling via vessel cooption, regression and growth in tumors. Journal of Theoretical Biology, Vol 241, 903-918.

[Baxter & Jain, 1989] Baxter, L. T. & Jain, R. K. 1989. Transport of fluid and macro-molecules in tumors i. role of intersititial pressure and convection. Microvascular Research, Vol 37, 77-104.

[Baxter & Jain, 1990] Baxter, L. T. & Jain, R. K. 1990. Transport of fluid and macro-molecules in tumors. ii. role of heterogeneous perfusion and lymphatics. Microvascular Research, Vol 40 (2), 246 – 263.

[Bentley et al., 2008] Bentley, K., Gerhardt, H. & Bates, P. 2008. Agent-based simulation of notch-mediated tip cell selection in angiogenic sprout initialisation. Journal of Theoretical Biology, Vol 250, 25-36.

[Cai et al., 2011] Cai, Y., Xu, S., Wu, J. & Long, Q. 2011. Coupled modelling of tumour angiogenesis, tumour growth and blood perfusion. Journal of Theoretical Biology, Vol 279, 90-101.

[Chreech et al., 1958] Chreech, O. J., Krementz, E. T. & Ryan, R. F. 1958. Chemotherapy of cancer: regional perfusion ultilizing an extracorporeal circuit. Ann Surg. Vol 148: 616-32.

[Decuzzi et al., 2009] Decuzzi, P., Pasqualini, R., Arap, W. & Ferrari, M. 2009. Intravascular delivery of particulate systems: does geometry really matter? Pharm Res, Vol 26 (1): 235-243.

[Frieboes et al., 2009] Frieboes, H., Edgerton, M., Fruehauf, J., Rose, F., Worrall, L., Gatenby, R., Ferrari, M. & Cristini, V. 2009. Prediction of drug response in breast cancer using integrative experimental/computational modeling. Cancer Res. Vol 69(10):4484-92.

[Frieboes et al., 2010] Frieboes, H., Jin, F., Chuang, Y., Wise, S., Lowengrub, J. & Cristini, V. 2010. Three-dimensional multispecies tumor growth-ii: tumor invasion and angiogenesis. J. Theor. Biol. Vol 264, 1254–1278.

[Frieboes et al., 2013] Frieboes, H. B., Wu, M., Lowengrub, J., Decuzzi, P. & Cristini, V. 2013. A computational model for predicting nanoparticle accumulation in tumor vasculature. PLoS ONE, 8, e56876.

[Fung, 1997] Fung, Y. C. 1997. *Biomechanics: circulation.* 2rd edition, Springer, University of California, San Diego.

[Hellstrom *et al.*, 2007] Hellstrom, M., Phng, L. & Gerhardt, H. 2007. Vegf and notch signaling: the yin and yang of angiogenic sprouting. Cell Adh Migr, Vol 1 (3), 133-6.

[Intaglietta *et al.*, 1996] Intaglietta, M., Johnson, P. C. & Winslow, R. M. 1996. Microvascular and tissue oxygen distribution. Cardiovascular Research, 32 (4), 632–643.

[Jackson, 2003] Jackson, T. 2003. Intracellular accumulation and mechanism of action of doxorubicin in a spatio-temporal tumor model. J Theor Biol, Vol 220, 201-13.

[Jain, 2005] Jain, R. K. 2005. Normalization of tumor vasculature: an emerging concept in antiangiogenic therapy. Science, Vol 307, 58-62.

[Jain & Stylianopoulos, 2010] Jain, R. K. & Stylianopoulos, T. 2010. Delivering nanomedicine to solid tumors. Nat. Rev. Clin.Oncol. Vol 7, 653-664.

[Jain *et al.*, 2007] Jain, R. K., Tong, R. T. & Munn, L. L. 2007. Effect of vascular normalization by antiangiogenic therapy on interstitial hypertension, peritumor edema, and lymphatic metastasis: insights from a mathematical model. Cancer Research, Vol 67, 2729-2735.

[Jakobsson *et al.*, 2009] Jakobsson, L., Bentley, K. & Gerhardt., H. 2009. Vegfrs and notch: a dynamic collaboration in vascular patterning. Biochemical Society Transactions, Vol 37, 1233-1236.

[Jong & Borm, 2008] Jong, W. H. D. & Borm, P. J. 2008. Drug delivery and nanoparticles: applications and hazards. Int J Nanomedicine. Vol 3(2): 133-149.

[Lee *et al.*, 2006] Lee, D.-S., Bartha, K. & Rieger, H. 2006. Flow correlated percolation during vascular remodeling in growing tumors. Physical Review Letter, Vol 96, 058104.

[Levick, 1987] Levick, J. R. 1987. Flow through interstitium and other fibrous matrices. Quarterly Journal of Experimental Phsyiology, Vol 72, 409-438.

[Lowengrub *et al.*, 2010] Lowengrub, J., Frieboes, H., Jin, F., Chuang, Y.-L., Li, X., Macklin, P., Wise, S. & Cristini, V. 2010. Nonlinear modeling of cancer: bridging the gap between cells and tumors. Nonlinearity, Vol 23, R1-R91.

[Macklin & Lowengrub, 2007] Macklin, P. & Lowengrub, J. 2007. Nonlinear simulation of the effect of microenvironment on tumor growth. J Theor Biol, Vol 245 (4), 677-704.

[Macklin & Lowengrub, 2008] Macklin, P. & Lowengrub, J. 2008. A new ghost cell/level set method for moving boundary problems: application to tumor growth.. J Sci Comput, Vol 35, 266-299.

[Macklin *et al.*, 2009] Macklin, P., McDougall, S., Anderson, A. R. A., Chaplain, M. A. J., Cristini, V. & Lowengrub, J. 2009. Multiscale modelling and nonlinear simulation of vascular tumour growth. Journal of Mathematical Biology, Vol 58, 765-798.

[McClaine *et al.*, 2012] McClaine, R. J., Giglia, J. S., Ahmad, S. A., McCoy, S. J. & Sussman, J. J. 2012. Quality of life outcomes after isolated limb infusion. Annals of Surgical Oncology, Epub.

[McDougall *et al.*, 2006] McDougall, S. R., Anderson, A. R. A. & Chaplain, M. A. J. 2006. Mathematical modelling of dynamic adaptive tumour-induced angiogenesis: clinical implications and therapeutic targeting strategies. Journal of Theoretical Biology, Vol 241, 564-589.

[McDougall *et al.*, 2002] McDougall, S. R., Anderson, A. R. A., Chaplain, M. A. J. & Sherratt, J. A. 2002. Mathematical modelling of flow through vascular networks: implications for tumour-induced angiogenesis and chemotherapy strategies. Bull. Math. Biol. Vol 64, 673-702.

[Noorda *et al.*, 2007] Noorda, E. M., van Kreij, R. H. & Vrouenraets, B. C. 2007. The health-related quality of life of long-term survivors of melanoma treated with isolated limb perfusion. Eur J Surg Oncol. Vol 33: 776-82.

[Owen *et al.*, 2004] Owen, M. R., Byrne, H. M. & Lewis, C. E. 2004. Mathematical modelling of the use of macrophages as vehicles for drug delivery to hypoxic tumour sites. Journal of Theoretical Biology, Vol 226 (4), 377 – 391.

[Pittman, 2011] Pittman, R. 2011. *Regulation of Tissue Oxygenation.* Morgan and Claypool Life Sciences, San Rafael (CA).

[Pries *et al.*, 1992] Pries, A. R., Neuhaus, D. & Gaehtgens, P. 1992. Blood viscosity in tube flow: dependence on diameter and hematocrit. Am J Physiol Heart Circ Physiol, Vol 263, H1770-H1778.

[Pries *et al.*, 1998] Pries, A. R., Secomb, T. W. & Gaehtgens, P. 1998. Structural adaptation and stability of microvascular networks: theory and simulations. Am J Physiol Heart Circ Physiol, Vol 275, H349-H360.

[Sanga *et al.*, 2006] Sanga, S., Sinek, J., Frieboes, H., Ferrari, M., Fruehauf, J. & Cristini, V. 2006. Mathematical modeling of cancer progression and response to chemotherapy. Expert Rev Anticancer Ther, Vol 6, 1361-76.

[Scallan *et al.*, 2010] Scallan, J., Huxley, V. & Korthuis, R. 2010. *Capillary Fluid Exchange: Regulation, Functions, and Pathology.* Morgan and Claypool Life Sciences, San Rafael (CA).

[Seeley *et al.*, 2004] Seeley, R. R., Stephens, T. D. & Tate, P. 2004. *Anatomy and Physiology.* 7rd edition, McGraw-Hill Science/Engineering/Math.

[Sinek *et al.*, 2004] Sinek, J., Frieboes, H., Zheng, X. & Cristini, V. 2004. Two dimensional chemotherapy simulations demonstrate fundamental transport and tumor response limitations involving nanoparticles. Biomed Microdev, Vol 6, 297-309.

[Sinek *et al.*, 2009] Sinek, J., Sanga, S., Zheng, X., Frieboes, H., Ferrari, M. & Cristini, V. 2009. Predicting drug pharmacokinetics and effect in vascularized tumors using computer simulation. Mathematical Biology, Vol 58, 485-510.

[Stephanou *et al.*, 2005] Stephanou, A., Mcdougall, S., Anderson, A. & Chaplain, M. 2005. Mathematical modelling of flow in 2d and 3d vascular networks: applications to anti-angiogenic and chemotherapeutic drug strategies. Mathematical and Computer Modelling, Vol 40 (10), 1137-1156.

[Swabb *et al.*, 1974] Swabb, E. A., Wei, J. & Gullino, P. M. 1974. Diffusion and convection in normal and neoplastic tissues. Cancer Res, Vol 34 (10): 2814-2822.

[Tasciotti *et al.*, 2008] Tasciotti, E., Liu, X., Bhavane, R., Plant, K., Leonard, A. D., Price, B., Cheng, M. M.-C., Decuzzi, P., Tour, J., Robertson, F. & Ferrari, M. 2008. Mesoporous silicon particles as a multistage delivery system for imaging and therapeutic applications. Nature Nanotechnology, Vol 3: 151-157.

[van de Ven *et al.*, 2013] van de Ven, A., Addollahi, B., Martinez, C., Burey, L., Landis, M., Chang, J., Ferrari, M. & Frieboes, H. 2013. Modeling of nanotherapeutics delivery based on tumor perfusion. New Journal of Physics, in press.

[van de Ven *et al.*, 2012] van de Ven, A., Wu, M., Lowengrub, J., McDougall, S., Chaplain, M., Cristini, V., Ferrari, M. & Frieboes, H. 2012. Integrated intravital microscopy and mathematical modeling to optimize nanotherapeutics delivery to tumors. AIP Advances, Vol 2, 011208.

[Welter *et al.*, 2008] Welter, M., Bartha, K. & Rieger, H. 2008. Emergent vascular network inhomogeneities and resulting blood flow patterns in a growing tumor. Journal of Theoretical Biology, Vol 250, 257-280.

[Welter *et al.*, 2009] Welter, M., Bartha, K. & Rieger, H. 2009. Vascular remodelling of an arterio-venous blood vessel network during solid tumour growth. Journal of Theoretical Biology, Vol 259 405-422.

[Welter *et al.*, 2010] Welter, M., Bartha, K. & Rieger, H. 2010. Physical determinants of vascular network remodeling during tumor growth. Eur. Phys. J. E, Vol 33, 149-163.

[Welter & Rieger, 2013] Welter, M. & Rieger, H. 2013. Interstitial fluid flow and drug delivery in vascularized tumors: a computational model. A Computational Model. PLoS ONE, Vol 8(8).

[Wise *et al.*, 2008] Wise, S., Lowengrub, J., Frieboes, H. & Cristini, V. 2008. Three-dimensional multispecies nonlinear tumor growthi model and numerical method. J. Theor. Biol. Vol 253, 524-543.

[Wu *et al.*, 2013] Wu, M., Frieboes, H. B., McDougall, S., Chaplain, M. A. J., Cristini, V. & Lowengrub, J. 2013. The effect of interstitial pressure on tumor growth : coupling with the blood and lymphatic vascular systems. Journal of Theoretical Biology, 320, 131–151.

Physiological Name	Parameter	Unit	Value and Ref.
agent transfer rate (out of vessels)	k_D	per s	0 in Fig.1-8
			5.73e-3 red curve in Fig.3 and right panel in Fig.5
			Ref.[Baxter & Jain, 1989]
agent transfer rate (back into vessels)	k_T	per s	0 in Fig.1-8
			5.73e-3 red curve in Fig.3 and right panel in Fig.5
			Ref.[Baxter & Jain, 1989]
tumor drug binding rate	λ_{uptake}	per s	0 in Fig.1-5
			0.002 in Fig.6-8
host drug binding rate	λ_{decay}	per s	0 in Fig.1-5
			0.001 in Fig.6-8
Agent diffusivity	D_D	μm^2 per s	0.048 in the host and 1.3 in the tumor Ref.[Baxter & Jain, 1989]
Drug effect	λ_{effect}	non-dimensional	0 in Fig.1-5
			1 in Fig.6-8
rate by cell mitosis	λ_M	per s	0.77e-5
lymph collapsing threshold	KL_{max}	1	1 left column in Fig. 1-2, red in Fig.4, 5-8
			2 green in Fig.4 and in 5
			3 blue in Fig.4 and in 5
interstitial hydraulic conductivity	K_i	μm^2 per pa·s	3.1e-2 (in the tumor), cyan curves in Fig.5, middle column in Figs.6,7, and blue, cyan and magenta curves in Fig.8 Ref. [Baxter & Jain, 1989]
			0.64e-2, all the others, Ref.[Baxter & Jain, 1989]
vascular hydraulic conductivity	K_{Vf}	μm per pa·s	2.1e-5 (in the tumor), black curves in Fig.5, right column in Figs.6,7, and green, cyan and magenta curves in Fig.8 Ref. [Baxter & Jain, 1989]
			0.27e-5, all the others, Ref.[Baxter & Jain, 1989]
osmotic pressure difference	$\omega(\pi_v - \pi_i)$	pa	667 (in the tumor) magenta curves in Fig.8
			1333, all the others, Ref.[Baxter & Jain, 1989]
osmotic reflection coefficient	K_O	1	0.95
Retardation factor	τ_F	1	1 [Swabb *et al.*, 1974]

Table 1: Key parameters in the simulations; further parameters are in [Wu *et al.*, 2013].
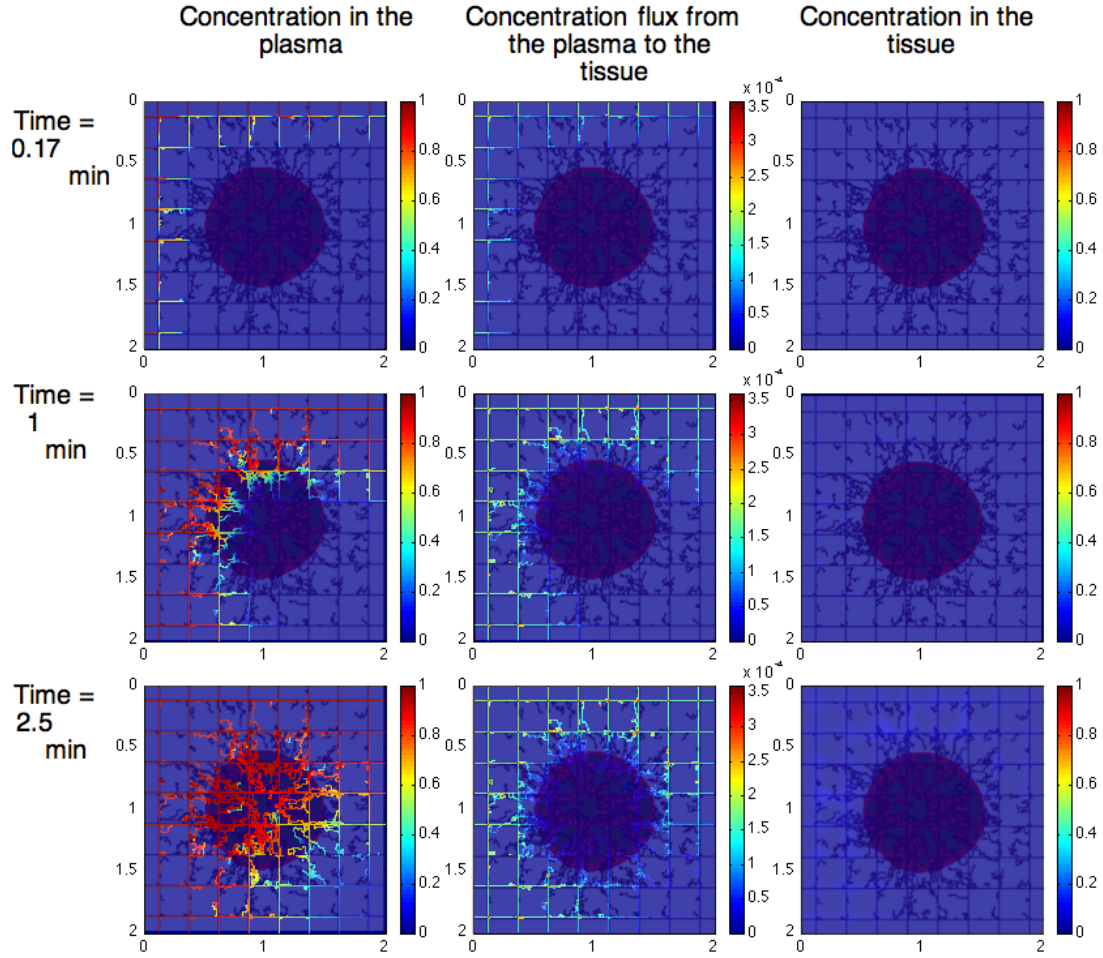
Figure 1: Agent distribution in the tumor tissue arising from constant injection at early times. Tissue is shown in a 2x2mm area: tumor with viable tissue in red, hypoxic in blue, and necrotic in brown, with the pre-existing vasculature (brown rectangular gridlines) as well as the neovasculature (irregular brown lines) originating in response to the net release of pro-angiogenic factors from the tumor hypoxic regions. The left column shows the concentration in the blood, the middle shows the transcapillary concentration flux, and the right shows the concentration in the tissue. Row 1 corresponds to $t = 0.17$ min, row 2 corresponds to $t = 1$ min and row 3 corresponds to $t = 2.5$ min. With only transcapillary convection ($k_T = k_D = 0$), the agent extravasation is small due to the hypertension in the tissue which impedes TFF.
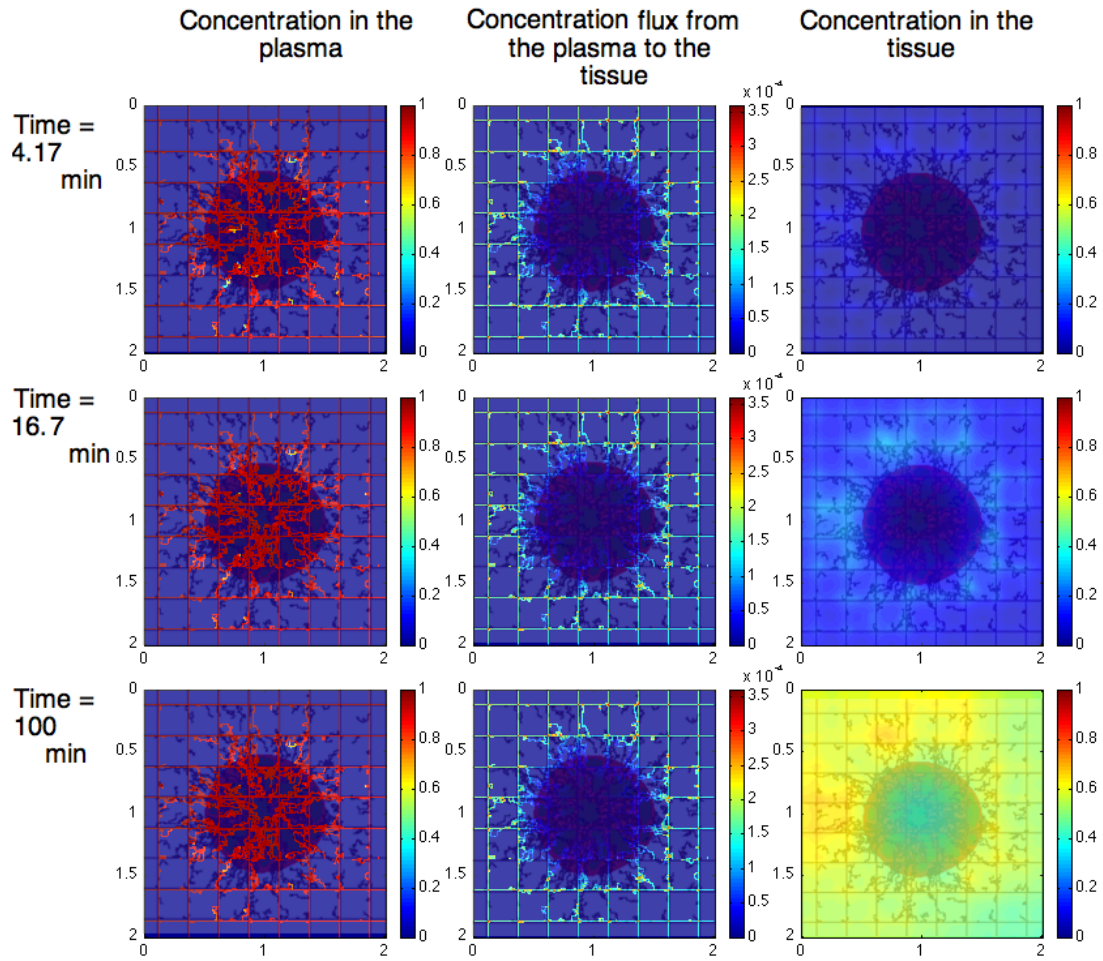
Figure 2: Agent distribution in the tumor tissue at later times. The left column shows the concentration in the blood, the middle shows the transcapillary concentration flux, and the right shows the concentration in the tissue. Row 1 corresponds to $t = 4.17$ min, row 2 corresponds to $t = 16.7$ min, and row 3 corresponds to $t = 100$ min. At $t = 4.17$ min, the agent concentration distribution in the blood reaches a homogeneous state which persists through $t = 100$ min. In row 3, the distribution of agent in the tissue shows a decrease in the tumor interior due to the lack of TFF.
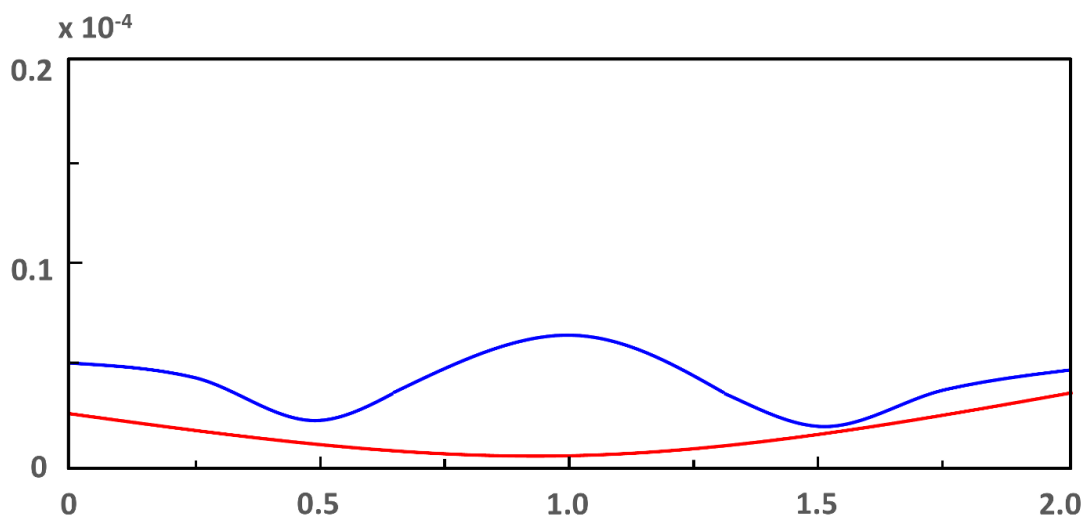
Figure 3: Concentration of agent with $k_T = k_D = 0$ in the tissue (cross section from the center) at $t = 100$ min. reveals a peak in the tumor region (blue curve) compared with the case when $k_T = k_D > 0$ (red curve).
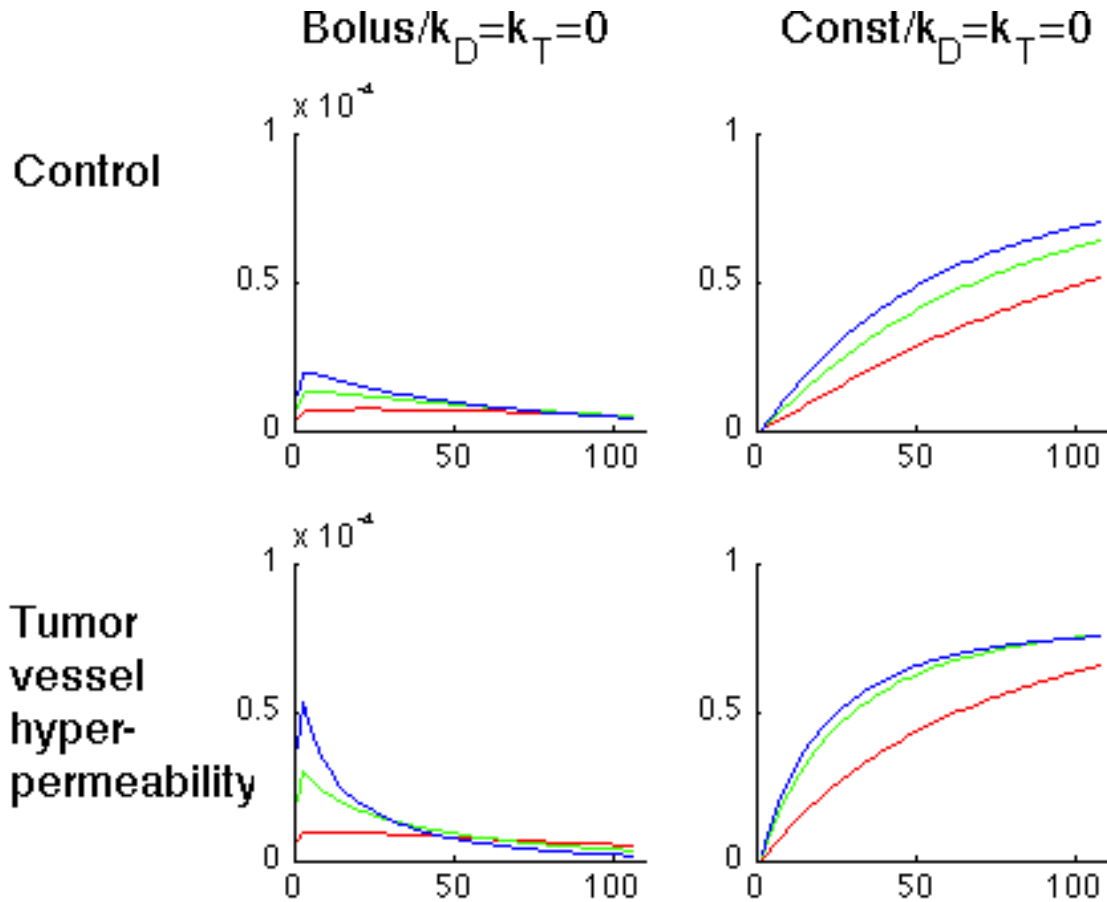
Figure 4: Average agent concentration (scaled by injection concentration) in the tumor vs. time (min.) shown in each subplot with lymphatic resistance $KL_{max} = 1$ in red, $KL_{max} = 2$ in green and $KL_{max} = 3$ in blue under bolus/constant (column 1/column 2) injection with/without (row 1/row 2) elevated vascular hydraulic conductivity. In all cases, a larger lymphatic resistance (i.e., $KLmax = 3$, blue curves) contributes to more rapid delivery to the tissue, which also contributes to a more rapid washout in the bolus injection case (column 1). For a lower lymphatic resistance (i.e., $KLmax = 1$, red curves), there is more drug in the tumor at later stages ($t > 50$ min) due to the inability of the drug to leave the tissue through either the vasculature or the lymphatics. The contrast between the two behaviors is accentuated with elevated vascular hydraulic conductivity (row 2 compared with row 1).
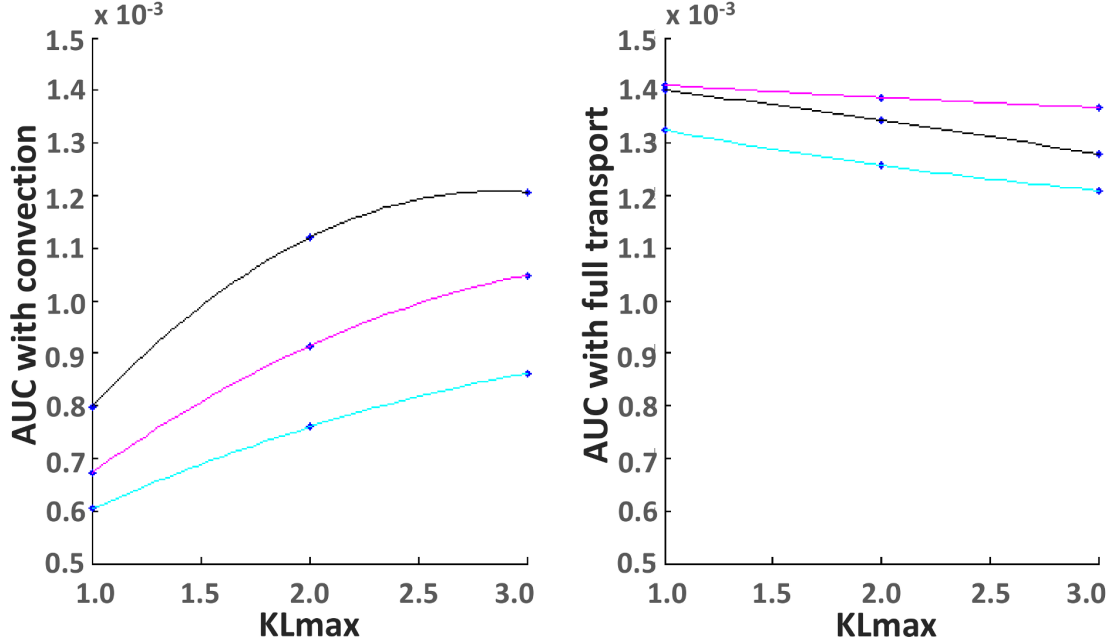
Figure 5: Agent availability in tumor tissue over time (area under the curve, AUC) after bolus injection with elevated vascular/interstitial hydraulic conductivity (black/cyan) compared with control (magenta) as a function of KL_{max} (x-axis). The left plot corresponds to convective transport of drug from the vasculature ($k_D = k_T = 0$) while the right plot considers other transport mechanisms ($k_D = k_T > 0$). In the convection only case (left), the AUC increases as KL_{max} for all cases while elevated vascular hydraulic conductivity contributes to a higher AUC. In addition, an elevated interstitial hydraulic conductivity contributes to lower AUC compared to the control. With additional transport (right), the AUC increases to a higher level in all cases but decreases as KL_{max} increases. The cases with elevated vascular/interstitial hydraulic conductivities exhibit lower AUC compared with the control. With an elevated interstitial hydraulic conductivity, the AUC is low with and without additional transport, which represents a transport impairment in general (cyan curve lies below the magenta and black curves). On the other hand, an elevated vascular hydraulic conductivity contributes to a higher AUC (black curve lies above the magenta curve) when the agent transport depends solely on convection. When there is elevated vasculature hydraulic conductivity, additional transcapillary transport, contributes to a lower AUC (black curve lies below the magenta curve).
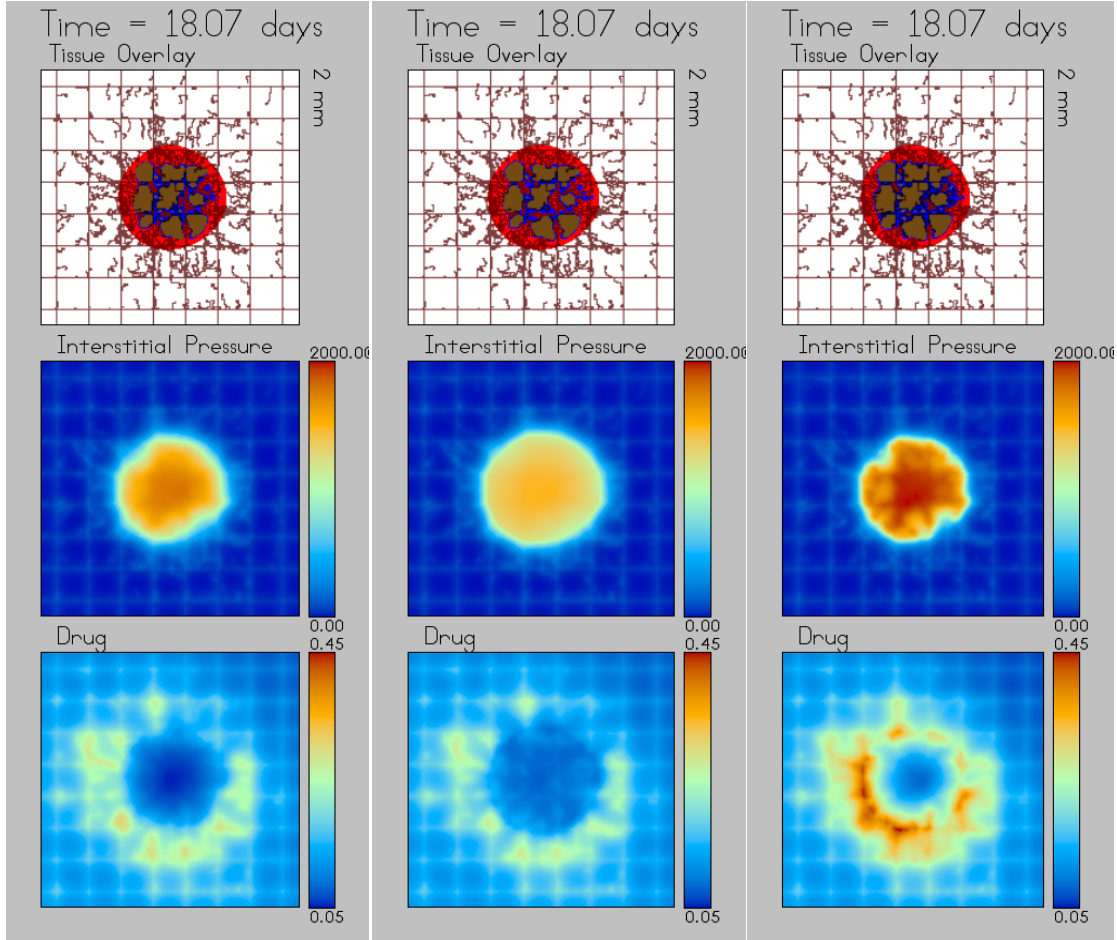
Figure 6: Tumor vasculature, IFP and the distribution of drugs before the tumor response at day 18.07. The tumor with elevated tumor interstitial hydraulic conductivity has a broad base plateau profile of IFP (Column 2, Row 2) whereas the IFP with elevated tumor vascular hydraulic conductivity (Column 3) is more hypertensive compared to the control (Column 1) due to excessive fluid extravasation. The broad base plateau profile contributes to a larger elevated IFP area and fluid flow away from the tumor [Wu *et al.*, 2013]. This decreases the drug concentration in and near the tumor (Column 2) while the plateau profile itself makes the drug distribution more uniform inside the tumor compared to the control (Column 2). Excessive fluid extravasation by an elevated tumor vascular hydraulic conductivity contributes to higher drug extravasation, thus increasing the concentration in the interstitium (Column 3), but the distribution is heterogeneous and the concentration in the tumor remains low (though higher than the base case).
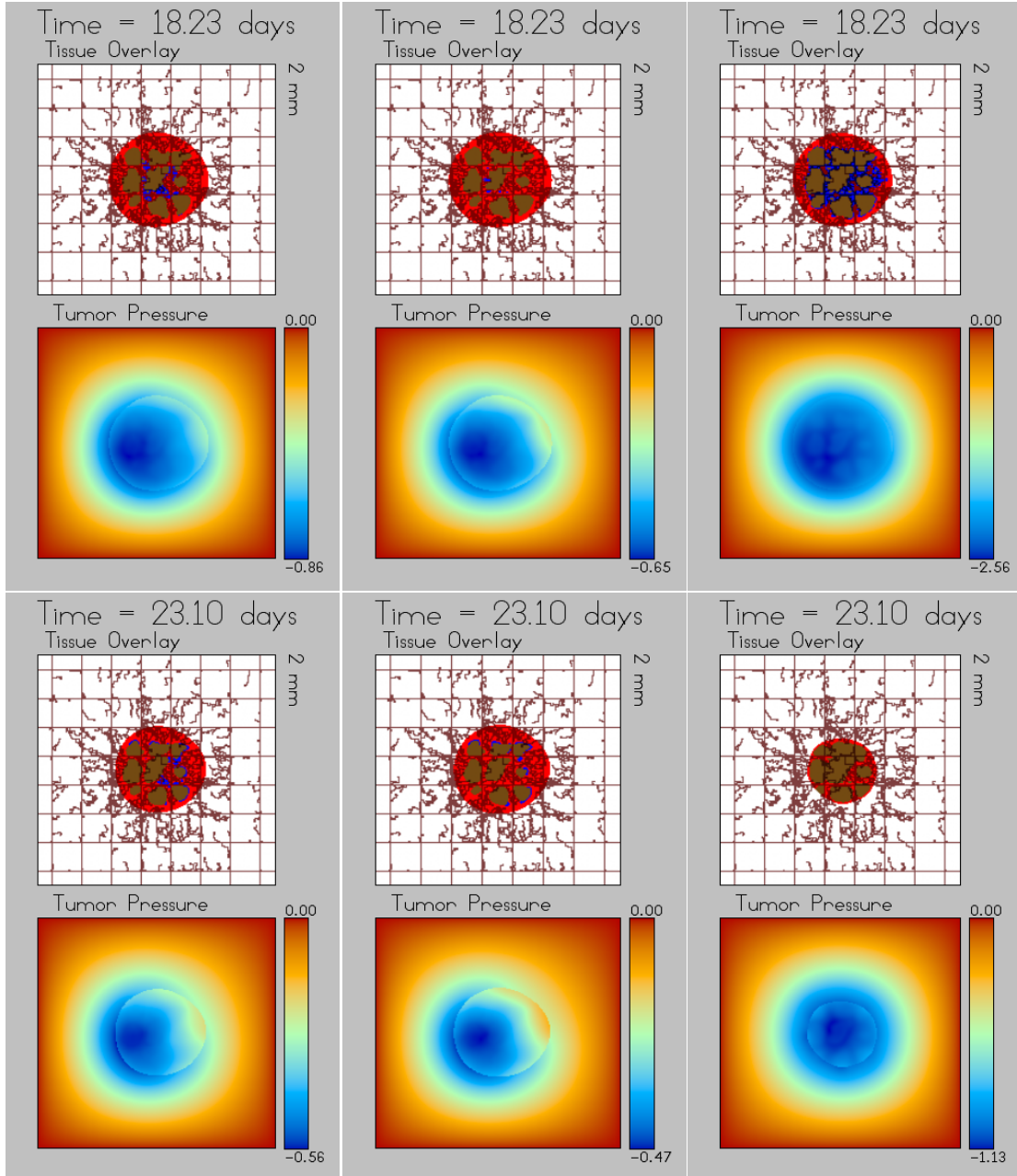
33

Figure 7: Tumor tissue, vasculature, and pressure with elevated vascular/interstitial hydraulic conductivities during treament with poorly-permeable ($k_D = k_T = 0$) drugs at high doses ($\lambda_{effect} = 1$) for day 18.23 until the end of the treatment at day 23.10. Although all the treated tumors have negative pressures due to cell death, those with elevated interstitial hydraulic conductivity maintain a higher pressure due to insufficient drug extravasation (Column 2 in Fig. 6). Tumors with elevated vascular hydraulic conductivity have the most negative pressure and shrink the most by day 23.10 due to higher agent concentration resulting from excessive fluid extravasation.
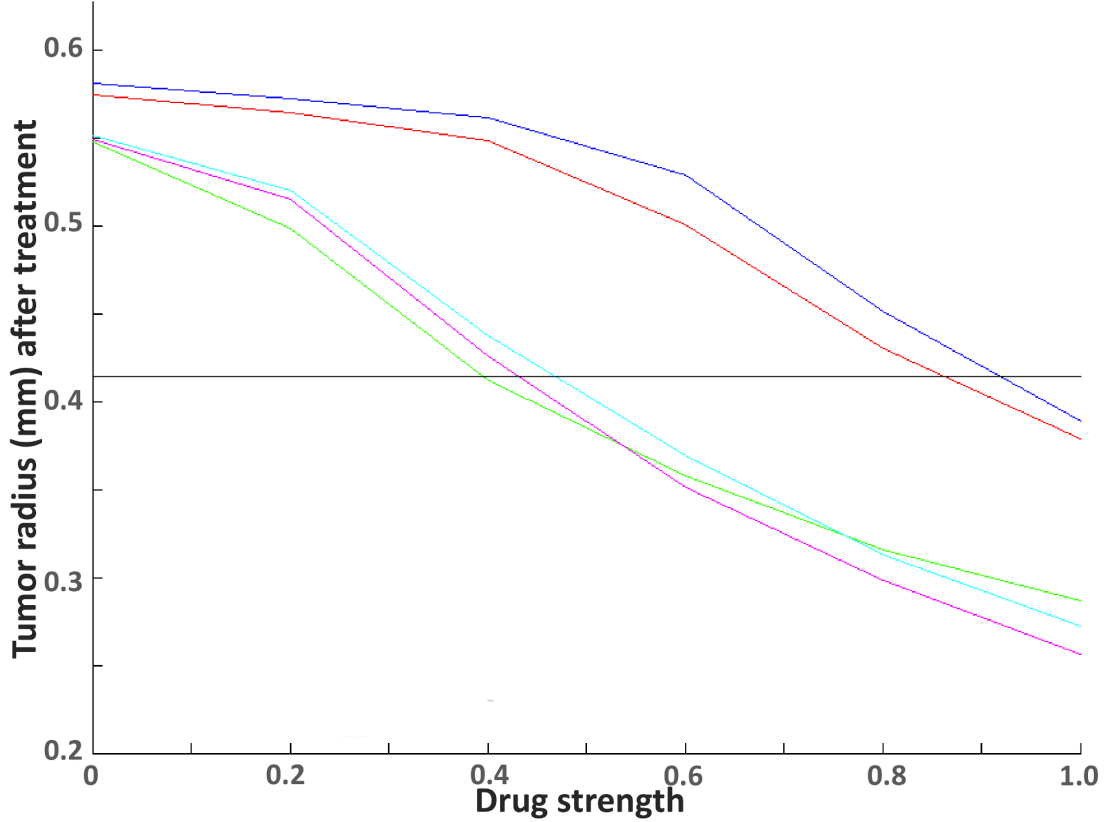
Figure 8: Tumor radius after ≈ 5 days of treatment by varying drug strength λ_{effect} from 0 to 1 (0 corresponds to an untreated tumor), with elevated vascular/interstitial hydraulic conductivity (green and blue, respectively), their combination (cyan curve), and their further combination with an attenuated transvascular osmotic pressure difference (magenta curve), compared to the control (red curve). The black horizontal line corresponds to the tumor radius before therapy. Tumors with elevated interstitial hydraulic conductivity (blue curve) do not shrink until the drug concentration increases to ~ 0.9, which is a slightly slower effect than the control (~ 0.85), due to the excessive fluid flow from the tumor into the surrounding tissue. Tumors with elevated vascular hydraulic conductivity (green curve) begin to shrink when the drug strength increases to ~ 0.45. However, with elevated vascular hydraulic conductivity alone, the shrinkage seems to saturate (green line) (note the transition between the green curve and the cyan or magenta curves), due to the heterogeneity and low drug concentration in the tumor interior. The tumor shrinkage slows down once the tumor radius $\lesssim 0.35$ mm.